Earth and Planetary Science Letters 543 (2020) 116349

Contents lists available at ScienceDirect

Earth and Planetary Science Letters

www.elsevier.com/locate/epsl

Dislocation interactions during low-temperature plasticity of olivine and their impact on the evolution of lithospheric strength

David Wallis [a,*,1], Lars N. Hansen [b,2], Kathryn M. Kumamoto [b], Christopher A. Thom [b], Oliver Plümper [a], Markus Ohl [a], William B. Durham [c], David L. Goldsby [d], David E.J. Armstrong [e], Cameron D. Meyers [f,3], Rellie M. Goddard [b], Jessica M. Warren [g], Thomas Breithaupt [b], Martyn R. Drury [a], Angus J. Wilkinson [e]

[a] Department of Earth Sciences, Utrecht University, Utrecht, 3584 CB, the Netherlands
[b] Department of Earth Sciences, University of Oxford, Oxford, OX1 3AN, UK
[c] Department of Earth, Atmospheric and Planetary Sciences, Massachusetts Institute of Technology, Cambridge, MA 02139-4307, USA
[d] Department of Earth and Environmental Science, University of Pennsylvania, Philadelphia, PA 19104, USA
[e] Department of Materials, University of Oxford, Oxford, OX1 3PH, UK
[f] Department of Earth Science, University of Minnesota-Twin Cities, Minneapolis, MN 55455, USA
[g] Department of Earth Sciences, University of Delaware, Newark, DE 19716, USA

ARTICLE INFO

Article history:
Received 17 September 2019
Received in revised form 5 May 2020
Accepted 14 May 2020
Available online xxxx
Editor: J. Brodholt

Keywords:
olivine
low-temperature plasticity
strain hardening
high-angular resolution electron backscatter diffraction (HR-EBSD)
microstructure
residual stress

ABSTRACT

The strength of the lithosphere is typically modelled based on constitutive equations for steady-state flow. However, strain hardening may cause significant evolution of strength in the colder load-bearing portion of the lithosphere. Recent rheological data from low-temperature deformation experiments on olivine suggest that strain hardening occurs due to the presence of temperature-independent back stresses generated by long-range elastic interactions among dislocations. These interpretations provided the basis for a flow law that incorporates hardening by the development of back stress. Here, we test this dislocation-interaction hypothesis by examining the microstructures of olivine samples deformed plastically at room temperature either in a deformation-DIA apparatus at differential stresses of ≤ 4.3 GPa or in a nanoindenter at applied contact stresses of ≥ 10.2 GPa. High-angular resolution electron backscatter diffraction maps reveal the presence of geometrically necessary dislocations with densities commonly above 10^{14} m^{-2} and intragranular heterogeneities in residual stress on the order of 1 GPa in both sets of samples. Scanning transmission electron micrographs reveal straight dislocations aligned in slip bands and interacting with dislocations of other types that act as obstacles. The resulting accumulations of dislocations in their slip planes, and associated stress heterogeneities, are consistent with strain hardening resulting from long-range back-stresses acting among dislocations and thereby support the form of the flow law for low-temperature plasticity. Based on these observations, we predict that back stresses among dislocations will impart significant mechanical anisotropy to deformed lithosphere by enhancing or reducing the effective stress. Therefore, strain history, with associated microstructural and micromechanical evolution, is an important consideration for models of lithospheric strength. The microstructural observations also provide new criteria for identifying the operation of back-stress induced strain hardening in natural samples and therefore provide a means to test the applicability of the flow law for low-temperature plasticity.

1. Introduction

Determining the strength of the lithosphere is a key objective in geodynamics and tectonics. The strength of the lithosphere is incorporated into models of processes including global convection (van Heck and Tackley, 2008), deformation in collision zones (England and Houseman, 1986; England and Molnar, 2015), and plate flexure beneath surface loads (Zhong and Watts, 2013) and in sub-

* Corresponding author.
E-mail address: dw584@cam.ac.uk (D. Wallis).
[1] Present address: Department of Earth Sciences, University of Cambridge, Cambridge, CB2 3EQ, UK.
[2] Present address: Department of Earth Science, University of Minnesota-Twin Cities, Minneapolis, Minnesota, 55455, USA.
[3] Present address: Department of Earth, Environmental, and Planetary Sciences, Brown University, Providence, Rhode Island, 02912, USA.

https://doi.org/10.1016/j.epsl.2020.116349

duction zones (Buffett and Becker, 2012; Hunter and Watts, 2016). Accordingly, the strength of the lithosphere is determined based on observations from each tectonic setting (e.g., Watts et al., 2013) and characterised in the form of rheological models with general applicability based on experimentally derived flow laws (e.g., Burov, 2011; Kohlstedt et al., 1995; Watts et al., 2013). These approaches indicate that in many settings the maximum stress that can be supported in a lithospheric section, and therefore much of the integrated strength, is likely controlled by low-temperature plasticity of olivine (Buffett and Becker, 2012; England and Molnar, 2015; Hansen et al., 2019; Hunter and Watts, 2016; Mei et al., 2010; Zhong and Watts, 2013). Low-temperature plasticity refers to deformation by dislocation glide described by an exponential flow law. This deformation mechanism is dominant under conditions at which long-range diffusion of point defects does not control the strain rate (e.g., Mei et al., 2010; Hansen et al., 2019).

Geophysical observations indicate that the strength of the lithosphere differs between tectonic settings. One proxy for lithospheric strength that provides a convenient metric to compare between regions is the elastic thickness (Walcott, 1970). Compilations of elastic thicknesses indicate that strength varies by an order of magnitude due to lithospheric structure and thermal regime in a manner broadly consistent with predictions from flow laws for steady-state deformation (Burov, 2011; Watts et al., 2013). However, recent models of flexure data have revealed differences in lithospheric strength that are difficult to reconcile based on conventional flow laws. For instance, lithospheric-strength profiles incorporating the flow law of Mei et al. (2010) for low-temperature plasticity of olivine provide good fits in models of continental shortening in the Tien Shan (England and Molnar, 2015) and of flexure of the Pacific plate at subduction zones (Hunter and Watts, 2016). However, Zhong and Watts (2013) found that profiles based on the flow law of Mei et al. (2010) overpredicted the strength of the lithosphere in models of flexure of the Pacific plate around Hawaiian seamounts. They found that the pre-exponential term in the flow law of Mei et al. (2010) must be reduced by a factor of 10^6–10^8 to reproduce the observed flexural response. Hunter and Watts (2016) suggested that subducting lithosphere is apparently strengthened as a result of unrelaxed viscoelastic stresses or that lithosphere at Hawaii is apparently weakened as a result of either bending stresses from plate cooling (Wessel, 1992) or magma assisted flexure (Buck et al., 2015).

Recent laboratory experiments have led to a new hypothesis regarding the cause of differences in lithospheric strength. Hansen et al. (2019) investigated low-temperature plasticity of single crystals and aggregates of olivine through experiments in a deformation-DIA (D-DIA) apparatus. Both single crystals and aggregates exhibited strain hardening of 1–2 GPa between the yield stress and steady-state flow stress. Importantly, Hansen et al. (2019) conducted experiments in which the samples were subjected to cycles of shortening and extension. These experiments revealed that the yield stress during the initial loading was consistently greater in magnitude than those on subsequent cycles. This behaviour, termed the Bauschinger effect, is widely recognised in the metallurgical literature and indicates that strain hardening arises, at least in part, from long-range elastic interactions among dislocations, termed kinematic hardening (e.g., Kuhlmann-Wilsdorf and Laird, 1979). These interactions manifest as back stresses among dislocations that reduce the apparent yield stress upon load reversal.

Based on these mechanical data, Hansen et al. (2019) formulated a flow law for low-temperature plasticity in olivine that characterises strain hardening by accumulation of back stress (σ_b). The flow law has the form

$$\dot{\varepsilon} = A \exp\left(-\frac{\Delta F}{RT}\right) \sinh\left(\frac{\Delta F}{RT}\frac{\sigma - \sigma_\mathrm{b}}{\Sigma}\right), \tag{1}$$

where $\dot{\varepsilon}$ is strain rate, A is a material-dependent prefactor, ΔF is the Helmholtz free energy, R is the gas constant, T is absolute temperature, σ is applied differential stress, and Σ is the intrinsic material resistance to dislocation glide. This resistance arises from that imparted by the structure of the lattice (σ_L) and that imparted by grain boundaries, which depends on the grain size (d), and is expressed as

$$\Sigma = \sigma_\mathrm{L} + K d^{-\frac{1}{2}}, \tag{2}$$

where K is a constant. Importantly, in Equation (1), the applied stress is modified by the back stress to give an effective stress ($\sigma - \sigma_\mathrm{b}$). The back stress evolves with plastic strain (ε_p) following the relation

$$\frac{\mathrm{d}\sigma_\mathrm{b}}{\mathrm{d}\varepsilon_\mathrm{p}} = \gamma\left[\sigma_{\mathrm{b,max}} - \mathrm{sgn}\left(\dot{\varepsilon}_\mathrm{p}\right)\sigma_\mathrm{b}\right], \tag{3}$$

where γ is a rate constant and $\sigma_{\mathrm{b,max}}$ is the maximum back stress. Lithospheric-strength profiles for 80 Myr-old oceanic lithosphere, that incorporate the flow law and are constructed for a range of strains, indicate that integrated lithospheric strength can potentially double over the first 2% strain, varying between values broadly consistent with those required in the models of flexure at Hawaiian seamounts at low strains and Pacific subduction zones at higher strains (Hansen et al., 2019).

Whilst clues to the microphysical mechanisms of strain hardening in olivine deforming by low-temperature plasticity can be gleaned from mechanical data, the key processes are yet to be characterised in detail based on microstructural observations. The similarity between strain hardening in single crystals and aggregates indicates that intragranular processes contribute to hardening in both cases (Hansen et al., 2019). Transmission electron microscope (TEM) images of olivine deformed at 600–1000 °C reveal cellular structures of tangled dislocations, inferred to contribute to strain hardening (Phakey et al., 1972; Druiventak et al., 2011, 2012). Recently, Kumamoto et al. (2017) used high-angular resolution electron backscatter diffraction (HR-EBSD) to detect densities of geometrically necessary dislocations (GNDs) on the order of 10^{14} m^{-2} around indents made at room temperature in single crystals of olivine. They inferred that interactions among the dislocations played a key role in strengthening the material. However, as the elastic analysis of Durinck et al. (2007) suggests that short-range interactions (e.g., formation of junctions) between dislocations may be weak in olivine, and previous studies have not mapped the stress fields associated with long-range elastic interactions, the contributions of these strengthening mechanisms to strain hardening remain unclear.

In the present study, we aim to test the validity of the flow law proposed by Hansen et al. (2019) (Eqns. (1)–(3)) against detailed microstructural analyses of samples deformed by low-temperature plasticity. Specifically, we test the validity of parameterising strain hardening in terms of the evolution of back stress (Eqn. (3)) against the observed distributions of dislocations and their associated stress fields. We focus on samples deformed at room temperature as this condition effectively excludes temperature-dependent processes (e.g., dislocation climb and diffusion creep), allowing the effects of relatively temperature independent processes (dislocation glide and associated stress fields) to be isolated and identified. We utilise samples deformed at room temperature in a D-DIA apparatus by Hansen et al. (2019) and in nanoindentation experiments by Kumamoto et al. (2017) to assess the processes operating in both sets of experiments. We employ HR-EBSD to simultaneously map densities of GNDs and heterogeneity in residual stress, along with scanning transmission electron microscope (STEM) images of dislocation arrangements. Finally, we make new predictions of the impact of back stresses among dislocations on the evolution

Table 1
Summary of samples, deformation experiments, and EBSD maps.

Sample	Experimental apparatus	Grain size (μm)	EBSD map size (pixels)	EBSD step size (μm)	Notes
MN1	Undeformed	> 1000	500 × 400	0.5	Single crystal typical of starting material for D-DIA and nanoindentation experiments
33	Undeformed	3.0	800 × 500	0.2	Isostatically hot pressed starting material for D-DIA experiments
PT-1184	Undeformed	42.9	400 × 316	0.5	Isostatically hot pressed starting material for D-DIA experiments
PI-1519	Paterson	4.6	800 × 600	0.2	Starting material for D-DIA experiments, previously deformed at temperatures of 1373–1523 K
San396b	D-DIA	7.7	–	–	Examples of diffraction patterns from a highly stressed (4.4 GPa) sample and after subsequent annealing
San423t	D-DIA	7.7	–	–	Example of the effect of annealing on pre-existing stresses at the beginning of an experiment
San382	D-DIA	∼ 700 and 3.0	2097 × 2051	0.5	Paired sample deformed at a temperature of 298 K, pressures of 5.3–8.2 GPa, and differential stresses of −3.8–4.3 GPa
San382t	D-DIA	∼ 700	295 × 155	0.15	Single crystal portion of San382
San382b	D-DIA	3.0	320 × 200	0.15	Aggregate portion of San382
San377b	D-DIA	42.9	–	–	Part of a paired sample deformed at a temperature of 298 K, pressures of 5.6–10.1 GPa, and differential stresses of < 4.3 GPa
OP4-2 300 nm	Nanoindentation	> 1000	90 × 90	0.1	Indent to a maximum depth of 300 nm in an undeformed single crystal. Yield stress was 10.5 GPa
OP4-2 800 nm	Nanoindentation	> 1000	210 × 210	0.1	Indent to a maximum depth of 800 nm in an undeformed single crystal. Yield stress was 10.8 GPa
PI-1488 600 nm	Nanoindentation	9.6	–	–	Indent to a maximum depth of 600 nm in an aggregate previously deformed at temperatures of 1373–1423 K. Yield stress was 10.2 GPa

of lithospheric strength based on modelling of a multistage deformation history.

2. Methods

2.1. Samples from deformation-DIA experiments

We analyse the microstructures of two starting materials and four deformed samples from the experiments of Hansen et al. (2019), selecting samples that span the range of grain sizes that they investigated. The experimental conditions and key data are summarised in Table 1. These experiments were conducted in a D-DIA apparatus housed on the 6-BM-B beamline of the Advanced Photon Source at Argonne National Laboratory. A synchrotron X-ray source was employed to measure bulk strain through radiography and to determine elastic lattice strain, and thus the stress state, through energy-dispersive X-ray diffraction. The deformation experiments were conducted at a temperature of 298 K, pressures of 5.3–10.1 GPa, and differential stresses up to 4.3 GPa.

Both starting materials that we analyse, PT-1184 and PI-1519, were fabricated by hot-pressing powdered San Carlos olivine at 1250 °C in a gas-medium apparatus. Sample PI-1519 was also deformed at 1100–1250 °C in a gas-medium apparatus, as part of the data set presented by Hansen et al. (2011), and therefore provides upper bounds on the GND densities and stress heterogeneities present prior to deformation in the D-DIA experiments. The grain sizes of samples PT-1184 and PI-1519, measured by the line-intercept method using EBSD maps, are 42.9 μm and 4.6 μm, respectively (Hansen et al., 2019), including a scaling factor of 1.5 (Underwood, 1970 pp. 80–93).

Hansen et al. (2019) performed an annealing stage of approximately 10 minutes, at a temperature of 1000 °C and a pressure of several GPa, at the start of each experiment, which served to relax the macroscopic differential stress and internal stress heterogeneity imparted during initial pressurisation. These stresses potentially arise from the slightly non-cubic geometry of the assembly, elastic anisotropy of olivine grains in crystalline aggregates, and the stress fields of dislocations. Fig. 1 presents examples of the effect of this annealing step on peak width in the X-ray diffraction patterns, which is a proxy for internal stress heterogeneity. These data were collected during recent experiments (Table 1) that followed the same procedure as those of Hansen et al. (2019). As a clear visual example of the effect of stress heterogeneity, Fig. 1a demonstrates the contrast between a diffraction pattern collected at room temperature at the end of the annealing treatment and another collected under an applied stress of 4.4 GPa in sample San396b. After annealing, the sample exhibits narrower peaks and a more distinct doublet of the {112} and {131} peaks than in the stressed state. In the stressed state, these closely-spaced peaks merge, as stress heterogeneity results in a range of lattice spacings. Fig. 1b demonstrates that differential stresses generated during initial pressurisation are fully relaxed before the start of the experiments. Fig. 1c documents the reduction in the widths of diffraction peaks to approximately constant values during the annealing stage, indicating relaxation of pre-existing stress heterogeneity within the samples. We collected HR-EBSD data from portions of PT-1184 and PI-1519 extracted prior to this annealing step and therefore the stress heterogeneities and GND densities present in those datasets provide upper bounds on those actually present at the beginning of each D-DIA experiment.

The samples from D-DIA experiments that we analyse, San377 and San382, both consisted of assemblies of two samples, with one stacked on top of the other and deformed simultaneously. We add the suffixes 'b' and 't' to the experiment names given by Hansen et al. (2019) to indicate samples that were located on the bottom and top of their assemblies, respectively. Sample San377b was shortened to a strain of 18%. Sample San382 was deformed in an experiment that imposed shortening, followed by extension, and then final shortening. During these cycles, the maximum strains

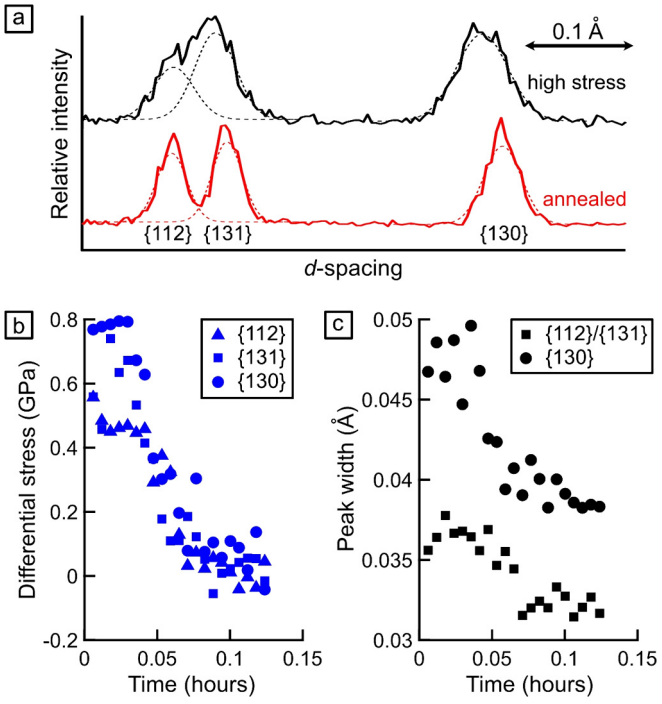

Fig. 1. Examples of the effects of annealing on X-ray diffraction patterns and macroscopic differential stresses. (a) Example diffraction patterns demonstrating the differences in peak width from a highly stressed sample and a sample in which internal stress has been reduced by annealing at 1000 °C at the beginning of a D-DIA experiment. (b) Differential stresses calculated from X-ray diffraction measurements of the d-spacings of three lattice planes, {*hkl*}, during annealing at 1000 °C at the beginning of a D-DIA experiment (San432). (c) Full width at half maximum of the peaks corresponding to the same three lattice planes. The widths of the {112} and the {131} peaks have been set as equal in the initial peak fitting as they form the doublet evident in (a) and are not always separable.

imposed on San382t and San382b were 13.5% and 8.4%, respectively.

Sections of the samples deformed in D-DIA experiments were prepared parallel to the loading column and near the centre of each sample. Both these samples and the starting materials were polished with successively finer diamond grits down to a grit size of 0.05 µm. The polished surfaces were coated with a layer of 0.5 nm thick Pt/Pd for EBSD mapping and 8 nm of Pt/Pd for focused ion beam scanning electron microscopy (FIB-SEM).

2.2. Samples from nanoindentation experiments

We analyse the microstructures of three indents from the experiments of Kumamoto et al. (2017). During nanoindentation experiments, dislocation motion can be activated at low temperatures due to confinement imposed by the sample material and indenter, which inhibits fracturing during loading (Swain and Hagan, 1976). Kumamoto et al. (2017) performed nanoindentation experiments at room temperature on an MTS Nanoindenter XP in the Department of Materials, University of Oxford, using a spheroconical diamond tip with an effective radius of 3.0 µm. Samples were polished with successively finer diamond grits and finished with 0.03 µm colloidal silica prior to nanoindentation. The maximum depths reached for the indents in OP4-2 were 300 nm and 800 nm, whereas the maximum depth reached for the indent in PI-1488 was 600 nm.

The starting materials for the nanoindentation experiments consisted of San Carlos olivine. Two of the indents that we analyse were in a gem-quality single crystal, sample OP4-2. The other indent was in an aggregate, sample PI-1488, that was isostatically hot-pressed and then deformed at a final temperature of 1150 °C by Hansen et al. (2011).

2.3. Microstructural analyses

2.3.1. Electron backscatter diffraction

EBSD data were acquired on field-emission gun SEMs at the University of Oxford, Utrecht University, and the Zeiss Microscopy Centre. All three instruments were equipped with Oxford Instruments Nordlys Nano or Symmetry detectors and AZtec acquisition software. Map dimensions are presented in Table 1. Reference-frame conventions were validated following the approach of Britton et al. (2016). For all (HR-)EBSD maps presented here, x_1 is horizontal, x_2 is vertical, and x_3 is out of the plane of the map. For HR-EBSD analysis, diffraction patterns were saved at a resolution of 1344 × 1024 pixels.

GND densities and residual-stress heterogeneities were calculated respectively from lattice rotations and elastic strains measured by the cross-correlation-based HR-EBSD postprocessing method of Wilkinson et al. (2006) and Britton and Wilkinson (2012, 2011). The cross-correlation procedure maps the shifts in 100 regions of interest within the diffraction patterns relative to their positions in a reference pattern within each grain to overdetermine the deformation gradient tensor describing lattice rotations and elastic strains. Densities of GNDs were calculated from the rotation fields following the method of Wallis et al. (2016). As the appropriate dislocation types to fit to the lattice curvature generated at low temperatures are not clear *a priori*, we present maps of the total dislocation density, which should be affected little by potential inaccuracies in the dislocation types used to fit the lattice curvature. Stress heterogeneities were calculated from the strain heterogeneities using Hooke's law and the elastic constants for olivine at room temperature and a confining pressure of 1 atm (Abramson et al., 1997).

Measured elastic strains and residual stresses are determined relative to the strain and stress state at the reference point in each grain. Reference points were chosen in areas of good pattern quality away from grain boundaries. In the maps of the indents in the previously undeformed single crystal, OP4-2, regions far from the indents are likely free from significant elastic strain, and therefore HR-EBSD provides maps of the absolute residual stresses around the indents. In contrast, no portion of the samples deformed in D-DIA experiments can be assumed to be strain-free. Therefore, the stress data from these samples were normalised by subtracting the mean of each component of the measured stress tensor within each grain, providing maps of relative stress heterogeneity (Wallis et al., 2019, 2017).

2.3.2. Focused ion beam and transmission electron microscopy

Electron-transparent foils were prepared using a FEI Helios Nanolab G3 Dualbeam FIB-SEM at Utrecht University. For samples deformed in D-DIA experiments, foils were oriented such that the plane of each foil was parallel to the maximum compression direction. For samples deformed in nanoindentation experiments, foils were oriented parallel to the indentation direction. Transmission electron microscope (TEM) investigations of the foils were carried out with an FEI Talos F200X operated at 200 kV. Bright-field and dark-field images were acquired simultaneously in STEM mode.

3. Results

3.1. Starting materials

Fig. 2 presents HR-EBSD maps of samples PT-1184 and PI-1519, typical of those used as starting materials for D-DIA experiments.

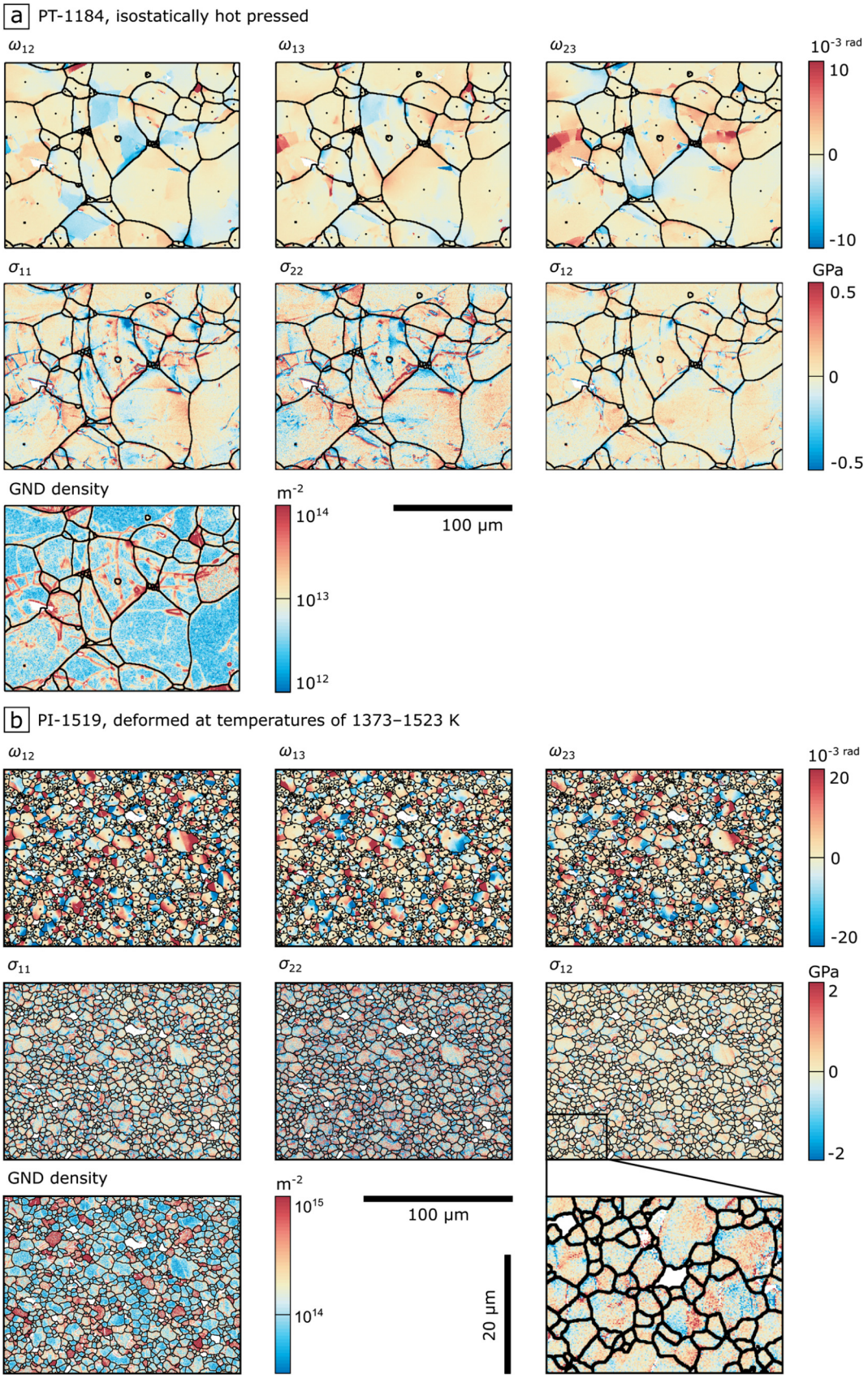

Fig. 2. HR-EBSD maps of lattice rotations (ω_{ij}), residual stress heterogeneity (σ_{ij}), and GND density in starting materials for D-DIA experiments. (a) Sample PT-1184, which was isostatically hot pressed but not deformed. (b) Sample PI-1519, which was isostatically hot pressed and then deformed at temperatures of 1373–1523 K by Hansen et al. (2011). Lattice rotations are relative to the crystal orientations at the reference points marked with black dots in each grain. Components of the residual stress tensor (σ_{ij}) are normalised to the mean of each component within each grain. (For interpretation of the colours in the figure(s), the reader is referred to the web version of this article.)

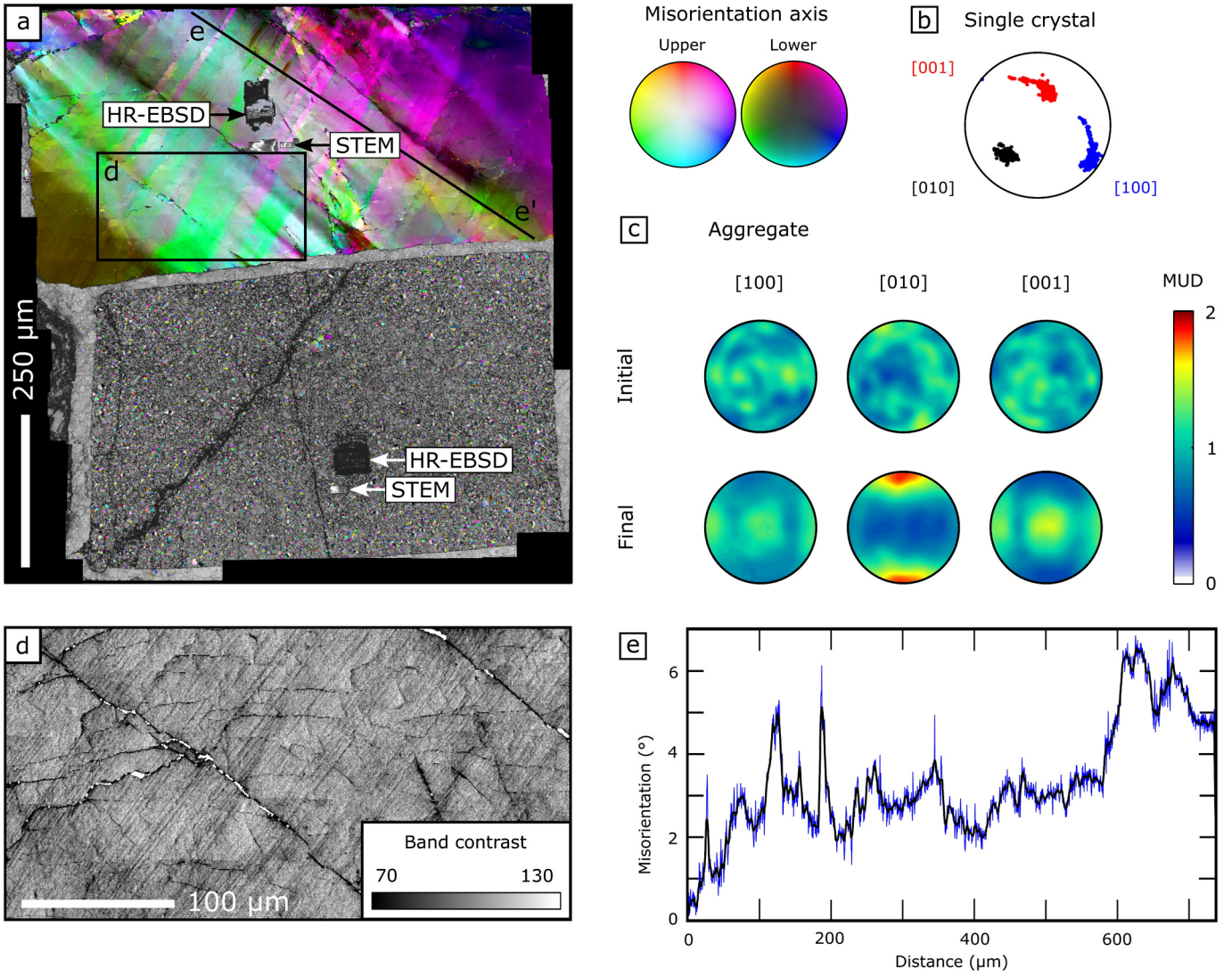

Fig. 3. EBSD data from experiment San382, which consists of a single crystal (San382t) stacked on top of an aggregate with a grain size of 3.0 µm (San382b). The initial compression direction is vertical in (a–d). (a) Overview EBSD map with olivine coloured by the misorientation axis between each point and the mean orientation of the grain. Areas not indexed as olivine are presented as greyscale band contrast. Annotations mark the areas where HR-EBSD data or liftouts for STEM imaging were acquired. (b) Pole figure presenting 50,000 randomly selected orientation measurements from the single crystal in the reference frame of the map in (a). (c) Pole figures of CPO in the starting material (sample 33, marked "Initial") and deformed aggregate (marked "Final") for San382b in the reference frame of the map in (a). Colours indicate multiples of uniform distribution (MUD). (d) Band contrast map of the area marked in (a). (e) Profile of misorientation angles relative to the first point along the profile marked e–e' in (a).

Maps of lattice rotations reveal subgrains as misoriented intragranular domains. The boundaries of these domains are evident as bands of elevated GND density representing subgrain boundaries. In the isostatically hot-pressed sample, PT-1184, apparent dislocation densities in subgrain interiors are on the order of 10^{12} m^{-2}, which corresponds to the density arising from noise in the rotation measurements (Wallis et al., 2016). In contrast, subgrain interiors in sample PI-1519, deformed at temperatures of 1373–1523 K by Hansen et al. (2011), contain elevated GND densities on the order of 10^{14} m^{-2}. Similarly, intragranular stress heterogeneities in PT-1184 have magnitudes on the order of a few hundred megapascals, whereas those in PI-1519 have magnitudes on the order of 1 GPa.

3.2. Samples deformed in deformation-DIA experiments

3.2.1. Electron backscatter diffraction

Fig. 3 presents EBSD data from experiment San382, which consists of a single crystal (San382t) stacked on top of an aggregate with a grain size of 3.0 µm (San382b). The single crystal was loaded in approximately the $[111]_c$ orientation, following the convention of Durham and Goetze (1977). Fig. 3a presents a map coloured by the misorientation axis (in the specimen reference frame) between the orientation at each pixel and the average orientation of each grain. This colour scheme reveals conjugate sets of diagonal bands with spacings on the order of tens of micrometers. A map based on the contrast of bands in the electron diffraction patterns (Fig. 3d) reveals bands with finer spacings of a few micrometers. A profile of misorientation angles across the single crystal (Fig. 3e) demonstrates that these banded structures are associated with misorientation angles up to a few degrees. Horizontal dark lines in Fig. 3d mark microfractures with spacings on the order of tens of micrometres. More prominent lines trending top-left to bottom-right mark a more widely spaced set of microfractures. Orientations within the single crystal are dispersed around [010] (Fig. 3b). Pole figures of crystal orientations within the aggregate (Fig. 3c) exhibit a maximum of [010] axes aligned with the compression direction, whereas [100] and [001] axes both exhibit two weaker maxima perpendicular to the compression direction. This distribution of crystal orientations contrasts with that

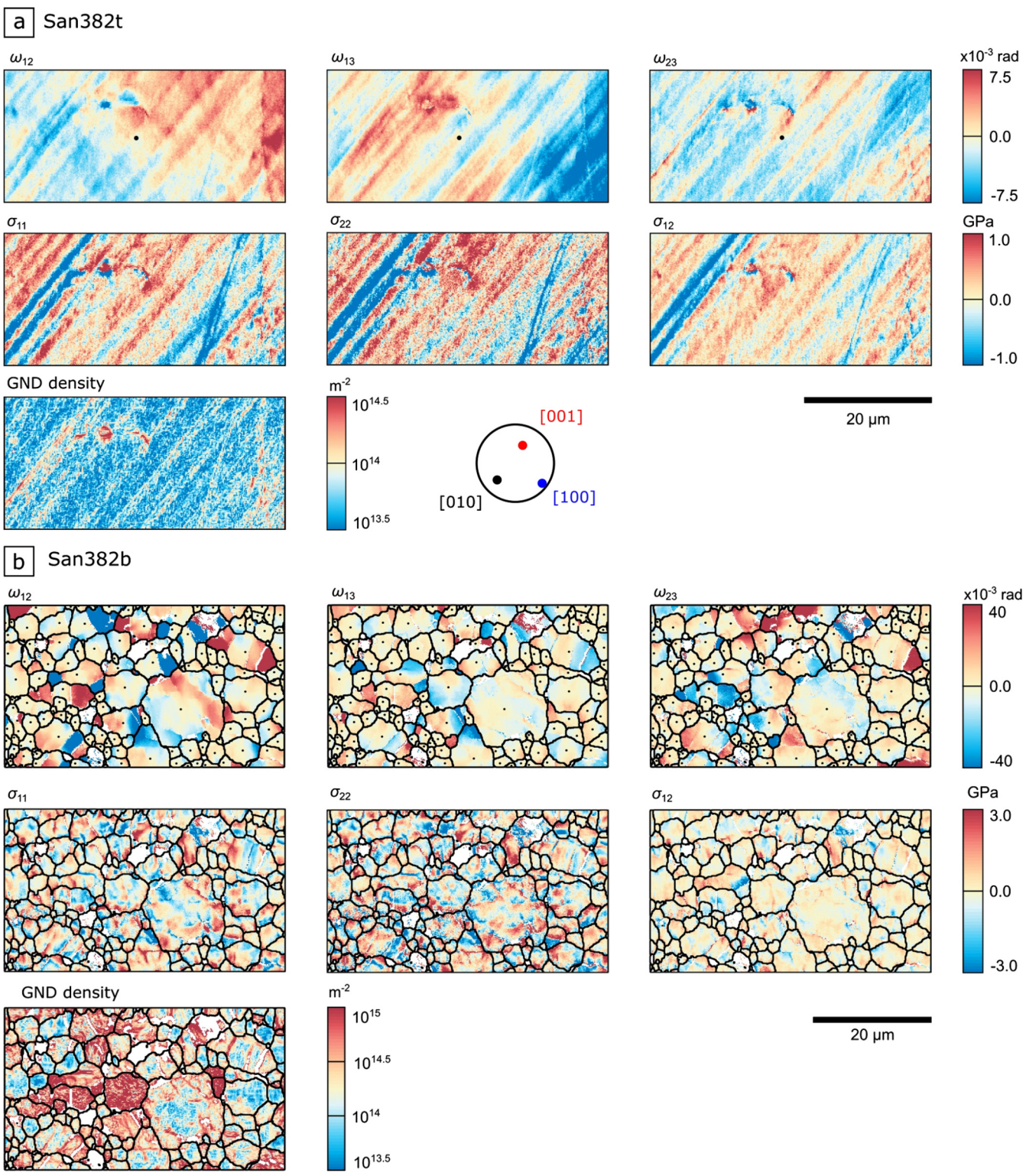

Fig. 4. HR-EBSD maps of lattice rotations (ω_{ij}), residual stress heterogeneity (σ_{ij}), and GND density in the single-crystal sample San382t (a) and aggregate San382b (b). The orientation of the single crystal in (a) is the same as presented in Fig. 3b. Rotations are relative to the crystal orientation at the reference points marked with black dots. Components of the residual stress tensor are normalised to the mean of each component within each grain. Tensional stresses are positive and compressional stresses are negative. The locations of the HR-EBSD maps are marked on the overview EBSD map in Fig. 3a.

of the starting material (Fig. 3c), which lacked a preferred orientation.

3.2.2. *High-angular resolution electron backscatter diffraction*

Fig. 4 presents HR-EBSD maps of samples San382t and San382b. The single crystal (San382t, Fig. 4a) exhibits linear domains, on the order of 1 µm in apparent width, in which the lattice is rotated on the order of 5×10^{-3} radians ($\sim 0.3\,^{\circ}$C) between domains. The sign of the lattice rotation alternates between domains. We refer to this microstructure as corrugated crystal lattice. The boundaries of each domain are marked by bands of elevated GND density, on the order of 10^{14} m^{-2}. Maps of residual stress heterogeneity ex-

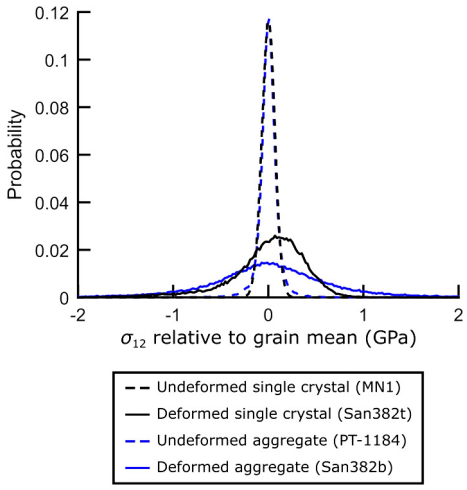

Fig. 5. Intragranular heterogeneity in the σ_{12} component of the residual stress tensor in undeformed and deformed single crystals and aggregates of olivine. Stresses are presented relative to the mean of the σ_{12} component within each grain.

hibit structures broadly similar to that of the lattice rotations. The σ_{11}, σ_{22}, and σ_{12} components vary in magnitude by ~ 1 GPa, and alternate in sign, over distances of approximately 1 μm.

The aggregate (San382b, Fig. 4b) exhibits even greater intragranular lattice distortion than the single crystal. Lattice rotations are typically on the order of 10^{-2} radians and GND densities commonly approach 10^{15} m^{-2}. Intragranular heterogeneities in the in-plane normal stresses typically have magnitudes of several gigapascals. Intragranular distortion within the aggregate lacks the linear, periodic structure evident in the single crystal.

Fig. 5 presents probability distributions of in-plane shear stress, σ_{12}, in undeformed and deformed single crystals and aggregates. The crystal-plasticity finite-element model predictions of Kartal et al. (2015) suggest that σ_{12} is the component of the stress tensor least modified by stress relaxation during sectioning. The undeformed single crystal (MN1) and undeformed aggregate (PT-1184, Fig. 2a) exhibit similar distributions, with standard deviations of 70 MPa and 140 MPa, respectively. The deformed single crystal (San382t, Fig. 4a) contains greater stress heterogeneity than the undeformed samples, with a standard deviation of 400 MPa. The deformed aggregate (San382b, Fig. 4b) displays the greatest intragranular stress heterogeneity, with a standard deviation of 790 MPa. As this sample has the smallest grain size and the greatest range of stress magnitudes, it has the greatest spatial gradients in stress.

3.2.3. Scanning transmission electron microscopy

Figs. 6a–c present STEM images of single crystal San382t. Dislocations in this sample form two perpendicular sets of structures trending along the diagonals of the micrographs, resulting in a cellular substructure (Figs. 6a and 6b). Both sets of structures consist of planar arrays of dislocations (Figs. 6b and 6c). Structures in which individual dislocations are visible reveal dislocations regularly spaced at intervals of < 100 nm (Fig. 6c). The characteristics (e.g., shape, diffraction contrast) of the structures are commonly different across the points at which the structures intersect, indicating changes in the densities or types of their constituent dislocations. White bands in Fig. 6a are microfractures aligned approximately parallel to the trace of the (100) plane.

Figs. 6d–f present STEM images of one grain in the coarse-grained aggregate San377b. Dislocations are homogeneously distributed and spaced approximately 100 nm apart. Dislocations typically contain straight segments a few hundred micrometers in length (Figs. 6d and 6f). Straight segments are often separated by shorter linking stepovers or curved segments (Figs. 6d and 6f), which, at their most dense, generate more chaotic dislocation networks and heterogeneous densities (Fig. 6e).

Figs. 6g–i present STEM images of the fine-grained aggregate San382b. As in the other two samples, dislocations are typically straight or gently curved, with occasional curved linking segments forming open networks. Elevated dislocation densities (Fig. 6g) and dislocation sources (below the bright pore in Fig. 6i) are present near grain boundaries. Diffraction-contrast fringes suggest that dislocations are split into partial dislocations bounding stacking faults (Fig. 6h).

3.3. Samples deformed in nanoindentation experiments

3.3.1. High-angular resolution electron backscatter diffraction

Fig. 7 presents HR-EBSD maps of nanoindents in the single crystal of olivine, OP4-2. The 300-nm indent (Fig. 7a) and the 800-nm indent (Fig. 7b) exhibit broad similarities in the distributions of lattice rotation, GND density, and residual stress around the indents. However, the magnitudes of these parameters and the size of the deformed zone are greater around the 800 nm indent. Sharp discontinuities in the rotation fields around the 800-nm indent mark the traces of microcracks formed during unloading (Kumamoto et al., 2017) and generate bands of elevated apparent GND density radiating from the indents. Broader zones of elevated GND density, reaching $> 10^{14}$ m^{-2}, surround each indent. Residual stresses adjacent to the indents exceed 1 GPa and decrease over distances of several micrometers. Residual stress fields also exhibit discontinuities across the traces of microcracks, indicating modification of the stress fields by fracturing.

3.3.2. Scanning transmission electron microscopy

Fig. 8 presents STEM images of cross sections through the indents. Figs. 8a–c and 8d–f reveal the distributions of dislocations beneath the indents in single crystal OP4-2, for which HR-EBSD maps are presented in Fig. 7. The indents in Figs. 8a–c and 8d–f had maximum depths of 300 nm and 800 nm, respectively. Beneath both indents, dislocations are contained within a volume approximately 5 μm wide and 4 μm deep. However, the dislocation density beneath the 800-nm indent (Fig. 8d and 8e) is higher than that beneath the 300-nm indent (Fig. 8a and 8b). Beneath both indents, dislocations are arranged in two sets of linear structures that appear approximately perpendicular to each other in the plane of the section. Based on the measured crystal orientations, one set of dislocations is arranged in a plane that contains the [100] direction, whereas the other set is likely arranged within the (100) plane. The densities of dislocations in these structures are highest near the surface impression of the indent and decrease with distance from the indent, revealing individual dislocations aligned along particular planes (Figs. 8a and 8d). Dislocation densities are locally elevated adjacent to intersections of the two sets of dislocations (e.g., bright dislocations near the centre of Fig. 8e). Outside the zones of influence of the indents, the crystal is free of dislocations (Figs. 8a and 8d).

Figs. 8g–i reveal the distribution of dislocations beneath an indent that proceeded to a maximum depth of 600 nm in a crystal containing pre-existing dislocations in sample PI-1488. Dislocations introduced by this indent occupy a volume approximately 3 μm wide and 2 μm deep and lack the orderly structure around the periphery of this zone (Fig. 8g) that is evident around the other two indents. Nonetheless, multiple sets of straight dislocations are discernable (Figs. 8h and 8i). Where these structures intersect the specimen surface, they produce steps that contribute to the residual impression (Figs. 8h and 8i).

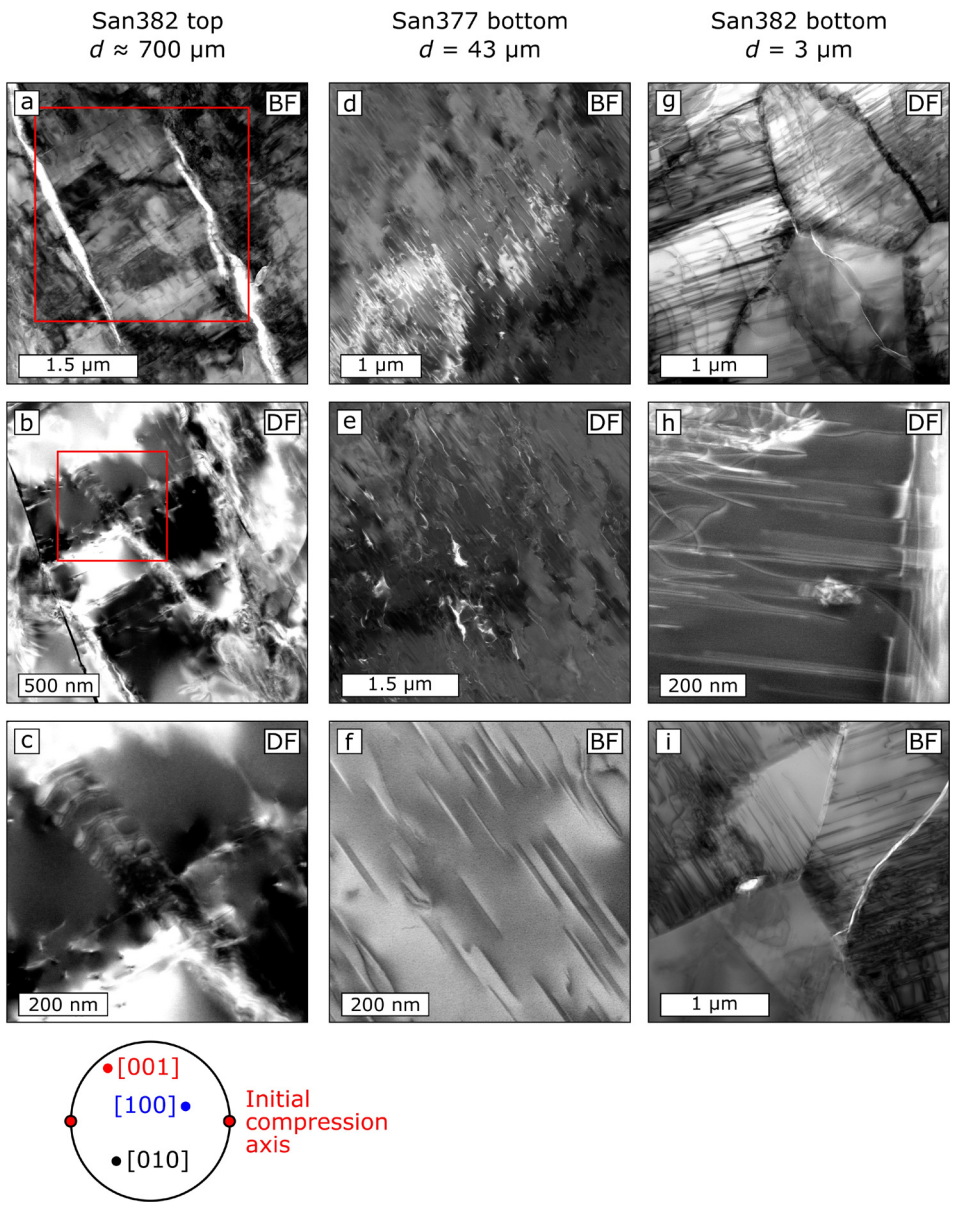

Fig. 6. STEM images of samples deformed in D-DIA experiments. Sample names and grain sizes, *d*, are given for each column. (a–c) and (g–i) correspond to the same samples for which HR-EBSD maps are presented in Fig. 4a and 4b, respectively, and the locations of the TEM lamellae are marked on the overview EBSD map in Fig. 3a. Red boxes in (a) and (b) indicate the areas of (b) and (c), respectively. The pole figure indicates the crystal orientation in (a–c). BF and DF indicate images taken in bright-field and dark-field modes, respectively.

4. Discussion

4.1. Deformation mechanisms

The (HR-)EBSD maps and STEM images provide constraints on the slip systems of dislocations active during low-temperature plasticity. The (HR-)EBSD data (Figs. 3a, 3d, 3e, and 4a) and STEM images of San382t (Fig. 6a–c), along with the STEM images of OP4-2 (Fig. 8a–f), contain dislocations aligned within two sets of structures that can be interpreted in terms of possible slip systems based on their crystal orientations, which gives similar results among the datasets. One set of structures is approximately parallel to the (100) plane, indicating dislocations on the (100)[001] slip system. This interpretation is consistent with orientations dispersed around the [010] axis in San382t (Fig. 3b). The other set of structures has a trace approximately parallel to that of either the (010) or (001) plane and therefore potentially result from slip bands of dislocations on the (010)[100], (010)[001] and/or (001)[100] slip systems. The alignment of [010] axes with the initial compression direction in the CPO of San382b also indicates the activity of the (010)[100] and/or (010)[001] slip systems. Previous TEM observations and analyses of slip bands expressed as deformation lamellae have also documented that the (100)[001] slip system, and particularly [001] screw dislocations, dominate at temperatures $< 900\,^{\circ}C$, with lesser activity of the {110}[001] system (Carter and Ave'lallemant, 1970; Druiventak et al., 2011; Gaboriaud et al., 1981; Idrissi et al., 2016).

In addition to sets of dislocations, dunites deformed at temperatures of a few hundred degrees Celsius often exhibit microfractures. Samples deformed at 300 °C by Druiventak et al. (2011) exhibited arrays of conjugate microfractures at angles of 30–45 °C to the shortening axis. Microcracks were also present in samples deformed at 600 °C by Druiventak et al. (2012). Those authors interpreted that the microfractures initiated during deformation as a consequence of work hardening associated with dislocation pile ups under conditions at which the differential stress typically ex-

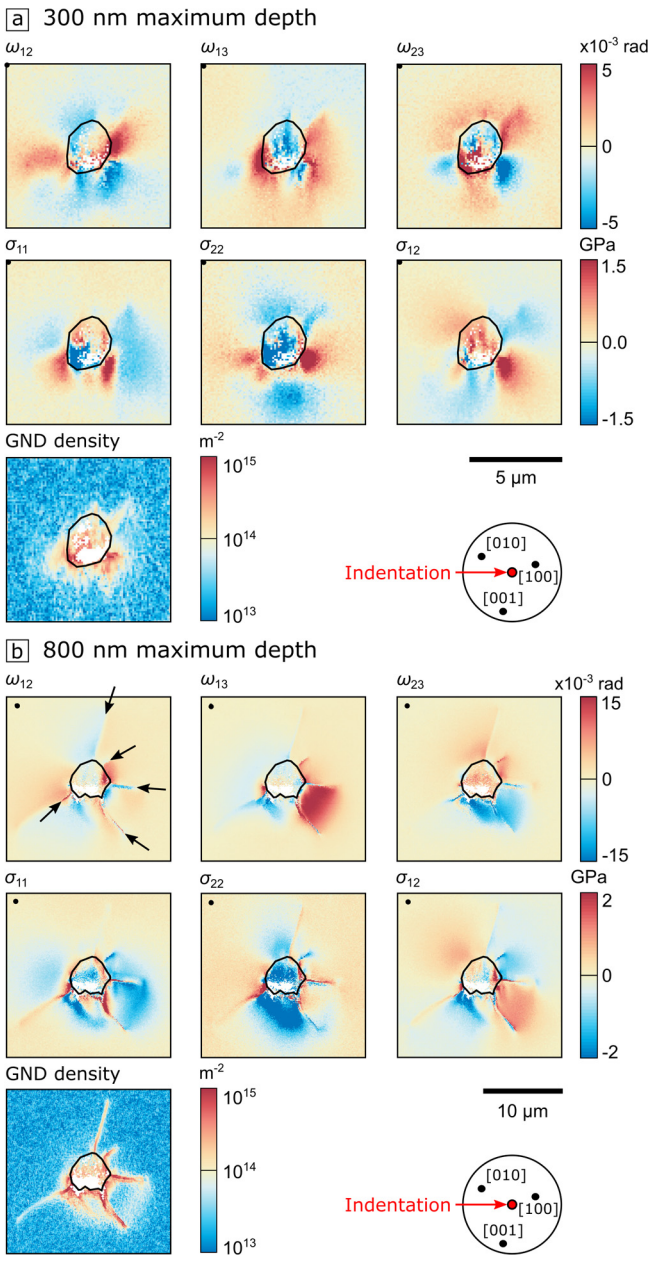

Fig. 7. HR-EBSD maps of lattice rotations (ω_{ij}), residual stress heterogeneity (σ_{ij}), and GND density around nanoindents in a single crystal of San Carlos olivine (sample OP4-2 of Kumamoto et al., 2017). (a) An indent that reached a maximum depth of 300 nm prior to unloading. (b) An indent that reached a maximum depth of 800 nm prior to unloading. Rotations and residual stresses are relative to the crystal orientation and stress state, respectively, at the reference points marked with black dots. Tensional stresses are positive and compressional stresses are negative. Black lines indicate the approximate outlines of the residual impressions. Black arrows in the map of ω_{12} in (b) mark the tips of the traces of microcracks. Pole figures indicate the crystal orientation and are the same for both indents.

ceeded the confining pressure (i.e., exceeded the Goetze criterion; Kohlstedt et al., 1995). In contrast, during the D-DIA experiments of Hansen et al. (2019), the differential stress remained below the confining pressure, suggesting that opening of fractures during deformation should be inhibited. The distributions of microfractures in sample San382t are consistent with this interpretation. The most common microfractures have traces perpendicular to the initial shortening direction (Fig. 3d) suggesting that they are mode I fractures opened during final depressurisation. The other, more widely spaced, set of microfractures (Fig. 3a and 3d) have traces parallel to those of one set of slip bands and therefore likely formed due to stresses around dislocations (Fig. 4). Mutual cross-cutting relationships between the two sets of fractures suggest that they both formed during depressurisation (Fig. 3d). Similarly, the nanoindentation introduced median (Fig. 8d and 8g) and lateral (Fig. 8d–g) cracks, which likely form during loading and unloading, respectively (Swain and Hagan, 1976). The latter process was also interpreted by Kumamoto et al. (2017) as having occurred during or after unloading. However, there is no indication that the median cracks significantly modified the dislocation behaviour as the cracks occur largely below the zones of dislocations (Fig. 8d and 8g).

4.2. Mechanisms of strain hardening and recovery

The microstructural data reveal several potential strain-hardening mechanisms. The TEM observations of Drury (1991) suggest that partial dislocations in olivine can pin other types of gliding dislocations, providing one potential source of hardening. Diffraction-contrast fringes in STEM images of dislocations generated in D-DIA experiments suggest that some dislocations are dissociated into partial dislocations bounding stacking faults (Fig. 6f and 6h). Poirier (1981) proposed that dislocations on the (100)[001] slip system can split into partial dislocations by the reaction

$$[001] = \frac{1}{12}[013] + \frac{1}{12}[0\bar{1}3] + \frac{1}{12}[013] + \frac{1}{12}[0\bar{1}3], \quad (4)$$

which does not require climb and results in partial dislocations that can all glide on (100) stacking-fault planes.

Details of the STEM images suggest that other short-range interactions among different types of dislocations added resistance to dislocation glide. Some dislocations contain short step-overs or S-shaped bends (sample San377b, Fig. 6d–f), similar to those produced by short-range interactions in dislocation dynamics simulations (e.g., Fig. 5 of Durinck et al., 2007). Even in the single crystal, San382t, the distribution of dislocations is heterogeneous, with intersecting bands of dislocations resulting in a cellular substructure (Fig. 6a–c). The cellular substructure is similar to those produced at temperatures of 600–800 °C in the experiments of Phakey et al. (1972) and Druiventak et al. (2012, 2011) and is commonly interpreted to result from local interactions among dislocations during strain hardening in a variety of materials (e.g., Kocks and Mecking, 2003). Differences in dislocation density across the intersections of slip bands beneath indents in sample OP4-2 (e.g., Fig. 8c and 8f) suggest that interactions between the two types of dislocation impeded their motion. This interpretation is supported by the smaller zone of elevated dislocation density beneath the 600-nm indent in the sample containing pre-existing dislocations (PI-1488, Fig. 8a) than beneath the 300-nm indent in the otherwise dislocation-free sample (OP4-2, Fig. 8g). Previous detailed TEM observations of single crystals of olivine deformed at temperatures of 600–1090 °C indicate that several short-range interactions contribute to strain hardening, including collinear interactions and formation of [101] and [10$\bar{1}$] junctions, along with the formation of dipoles (Mussi et al., 2017; Phakey et al., 1972).

Whilst short-range interactions potentially initially impeded dislocation glide, the observation of the Bauschinger effect by Hansen et al. (2019) indicates that hardening is dominated by long-range elastic interactions. This interpretation is supported by the observation of heterogeneous residual stresses (Figs. 4 and 7) that span a greater range of magnitudes than in the starting materials (Fig. 5). The residual stresses in the single crystal are particularly informative as they lack a contribution from grain compatibility during decompression and their relationship to the dislocation structures is particularly clear. Bands of residual stress, about 1 μm wide, 1 GPa in magnitude, and alternating in sign,

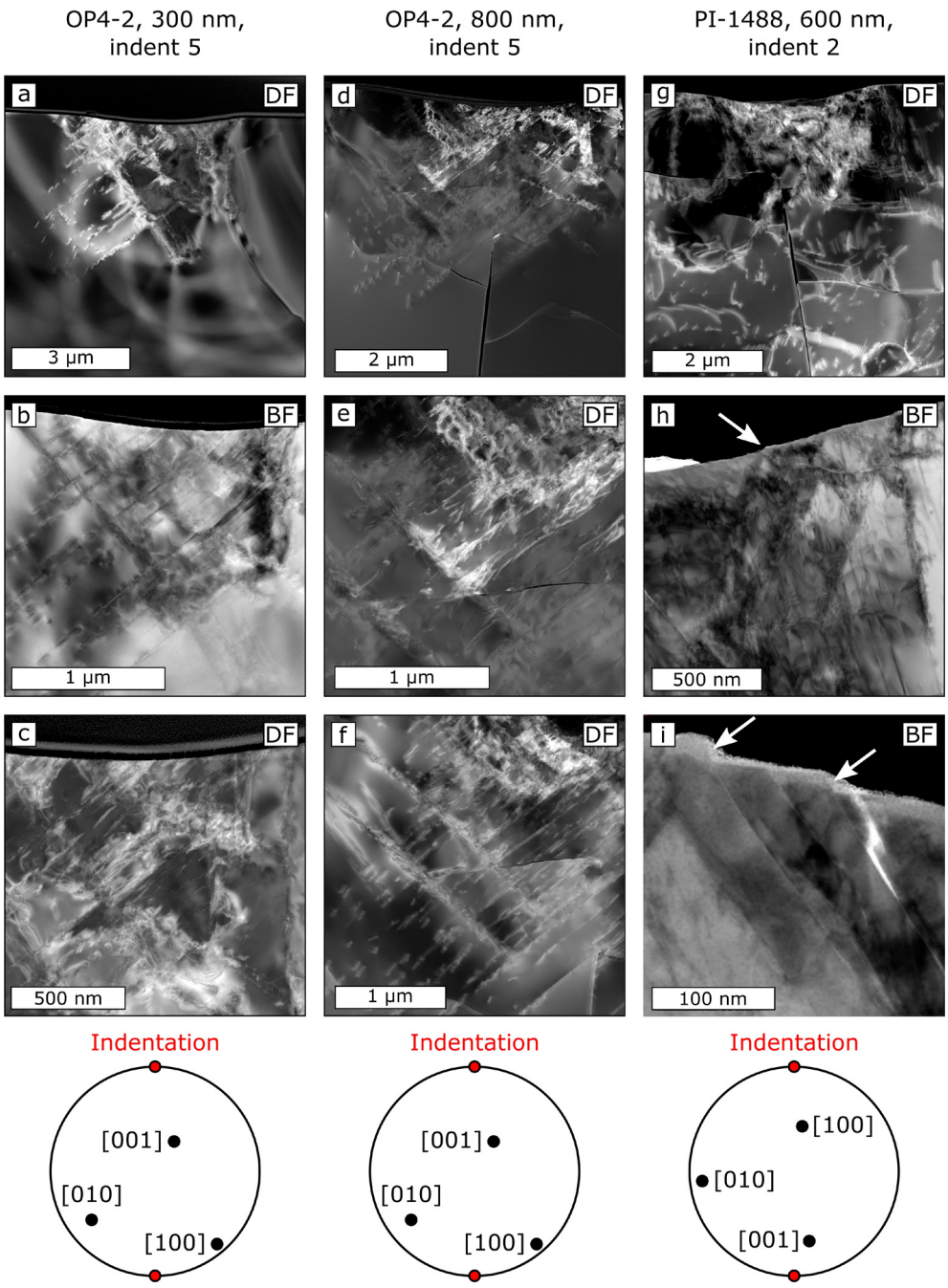

Fig. 8. STEM images of cross sections through nanoindents. Sample names, maximum indentation depths, and indent numbers are listed at the top of each column. Residual indents are evident as gentle curvature of the specimen surfaces near the tops of the images. Images in (e) and (f) display the same area at different diffraction conditions, where (e) portrays the change in contrast across the central slip band, while (f) reveals the individual dislocations. Arrows in (h) and (i) indicate steps in the surface of the residual indent. Pole figures indicate the crystal orientation in each column and are in the same reference frame as the STEM images. The crystal orientations of (a–c) and (d–f) are the same as these indents were in the same crystal. HR-EBSD maps of the indents in (a–c) and (d–f) are presented in Fig. 7a and 7b, respectively. BF and DF indicate images taken in bright-field and dark-field modes, respectively.

coincide with bands of rotated lattice and elevated GND density (Fig. 4a) that mark the locations of slip bands (Fig. 6a–c). These stress heterogeneities are characteristic of back stresses among dislocations piled up along their slip planes (e.g., Guo et al., 2014) and indicate a component of kinematic hardening, in which dislocations interact through their long-range stress fields (Kassner et al., 2013). These long-range interactions may contribute to the organisation of the substructure (Montagnat et al., 2006; Wallis et al., 2017), creating wavelengths up to several tens of micrometres in the misorientation associated with slip bands (Fig. 3a, 3d, 3e). The stress distributions in the aggregate are broadly consistent with this model but also contain a contribution from stresses imparted by anisotropic expansion of the grains during decompression. Similarly, the nanoindents are surrounded by zones of elevated GND density and stresses up to approximately 1 GPa in magnitude, which have been inferred to control strength, through long-range dislocation interactions, during indentation (Kumamoto et al., 2017; Nix and Gao, 1998).

The transition from hardening to constant flow stress in D-DIA experiments indicates the operation of one or more recovery processes even at room temperature (Hansen et al., 2019). Recovery mechanisms involving long-range diffusion, such as dislo-

cation climb, are kinetically inhibited at room temperature. Nes (1997) suggested that dislocation climb may contribute to dynamic recovery, even at low temperatures, if short-range diffusion is driven by locally high stresses. An alternative recovery mechanism is dynamic recovery by annihilation or other rearrangement of dislocations driven by the (local) applied stress (Kocks and Mecking, 2003; Nes, 1997). Cross slip of screw dislocations plays an important role in dynamic recovery of calcite (De Bresser, 2002) and metals (Essmann and Mughrabi, 1979). Phakey et al. (1972) inferred the operation of cross slip based on TEM observations of dislocation geometries in olivine deformed at temperatures $\geq 800\,^{\circ}C$ at a pressure of 1 GPa, but evidence for cross slip at 600 °C was lacking. However, cross slip may have been promoted by the higher confining pressures and differential stresses of our experiments (Poirier and Vergobbi, 1978; De Bresser, 2002). Similarly, stress-driven dynamic recovery will generally become more active with the rising applied stress during strain hardening until a constant flow stress is attained.

4.3. Implications for rheological models and lithospheric strength

The microstructures of samples deformed in D-DIA and nanoindentation experiments provide critical tests of models of low-temperature plasticity. The heterogeneous residual stresses, and their spatial relationship to areas of elevated GND density, in both single crystals and aggregates (Figs. 4 and 5), are consistent with the interpretation of Hansen et al. (2019) that strain hardening and the Bauschinger effect result from kinematic hardening induced by long-range dislocation interactions. Similarly, the distributions of dislocations and associated stress fields around nanoindents (Figs. 7 and 8) suggest that the same processes control the strain hardening observed in the spherical nanoindentation experiments of Kumamoto et al. (2017). The evidence for dislocation interactions influencing dislocation motion beneath the indents is also broadly consistent with models of the indentation size effect, in which yield stress and flow stress are inversely proportional to the size of spherical indenters or the depth of pyramidal indents, respectively (Kalidindi and Pathak, 2008; Nix and Gao, 1998). This effect was demonstrated to occur in olivine by Kumamoto et al. (2017). Those models suggest that smaller deforming volumes result in higher GND densities and stronger interactions among dislocations, which act against the applied stress (Nix and Gao, 1998).

The results of this study support the suggestion of Hansen et al. (2019) that strain hardening is an important consideration for models of lithospheric strength. One example in which such effects may be important is the difference between the strength of the Pacific plate at Hawaii (Zhong and Watts, 2013) and at the locations at which it enters subduction zones (Hunter and Watts, 2016). The model of Hansen et al. (2019) explains this strength difference in terms of strain hardening due to the accumulation of back stresses between dislocations, with greater strains and therefore hardening where the plate bends into subduction zones. The present study demonstrates that the model is consistent with the microstructures of the samples upon which it is based.

An additional prediction of the model of Hansen et al. (2019) is that the strength of lithosphere that has undergone strain hardening will be anisotropic. Accumulation of back stress during strain hardening reduces the yield stress during deformation of the opposite sense when the sign of the macroscopic stress is reversed. This effect, the Bauschinger effect, is evident in the mechanical data of Hansen et al. (2019) and is consistent with the stress heterogeneities generated by the dislocation content mapped in this study (Fig. 4). Anisotropic lithospheric strength has been inferred from studies of lithospheric flexure in a variety of tectonic settings (Audet and Bürgmann, 2011), although the validity of the methods used to detect it has been questioned (Kirby and Swain, 2014). Commonly, the orientation with the lowest apparent flexural strength is perpendicular to the strike of structures resulting from past compression, i.e., when the bending moment vector is parallel to strike (Audet and Bürgmann, 2011; Audet and Mareschal, 2004; Simons and van der Hilst, 2003). Regardless of the validity of the methods used in flexure studies, the model presented here and by Hansen et al. (2019) predicts that the strength of the lithosphere in deformed regions may be anisotropic in the sense inferred from flexure. An episode of shortening will result in accumulation of back stress, which may be retained in the cold, shallow lithosphere. If subsequent deformation induces extension in the shallow lithosphere along the former compression direction, then the apparent yield stress may be reduced relative to that in other orientations.

To provide a quantitative example of the effect of back stresses among dislocations in generating anisotropic lithospheric strength, we consider (for simplicity) oceanic lithosphere subjected to shortening followed by extension. In the calculation, both phases of deformation occur at absolute strain rates of 10^{-14} s^{-1}. To provide a simple example of the basic effect, we consider only the behaviour of olivine and omit other compositional and structural effects that will be present in nature. We employ the constitutive equations of Hansen et al. (2019) and explicitly link the mechanical behaviour to microphysical processes based on our new microstructural observations.

Fig. 9 presents depth profiles of the strength evolution of oceanic lithospheric. During initial shortening, the generation of back stresses among dislocations causes strain hardening in the portion of the lithosphere that initially deformed by low temperature plasticity (Fig. 9a). This hardening leads to the onset of either microcracking or dislocation creep in the middle and lower lithosphere, respectively, over the first 2% plastic strain. These transitions limit the amount of back-stress induced hardening that can occur at a particular depth. This portion of the deformation history is similar to that proposed for calcite by Meyer et al. (2019) but with the strain hardening mechanism identified and quantified.

The strength evolution during extension is controlled by the back stress stored during initial compression. In the middle lithosphere, at depths of approximately 30–60 km, the back stress stored during the shortening phase is sufficient that this portion of the lithosphere can yield in extension whilst still under compressional macroscopic stress (Fig. 9b). Whereas the integrated strength at the end of shortening is 2.4×10^{13} Nm^{-1}, the initial strength in extension is only 1.5×10^{13} Nm^{-1}. Put another way, plastic extension can commence whilst the lithosphere is still under approximately two thirds of the compressional load. At the microscale, the back stresses prime the dislocations to glide in the opposite direction upon reversal of the deformation and thereby reduce the effective stress ($\sigma - \sigma_b$ in Eqn. (1)). With increasing extensional strain, the middle lithosphere hardens in the sense opposite to that during shortening as dislocations glide, pile up, and accumulate back stress in the opposite direction.

Characterisation of the microstructures formed by low-temperature plasticity of olivine, particularly with the novel application of HR-EBSD, provides a new set of diagnostic microstructures with which to identify its past occurrence in natural samples (e.g., Matysiak and Trepmann, 2012). Specifically, straight dislocations confined within slip bands are associated with stress heterogeneities with magnitudes of several tens of percent of the macroscopic applied stress. Notably, such stress fields provide a microstructural indicator for the occurrence of kinematic hardening in natural samples and may be used to test the applicability of models such as that presented above.

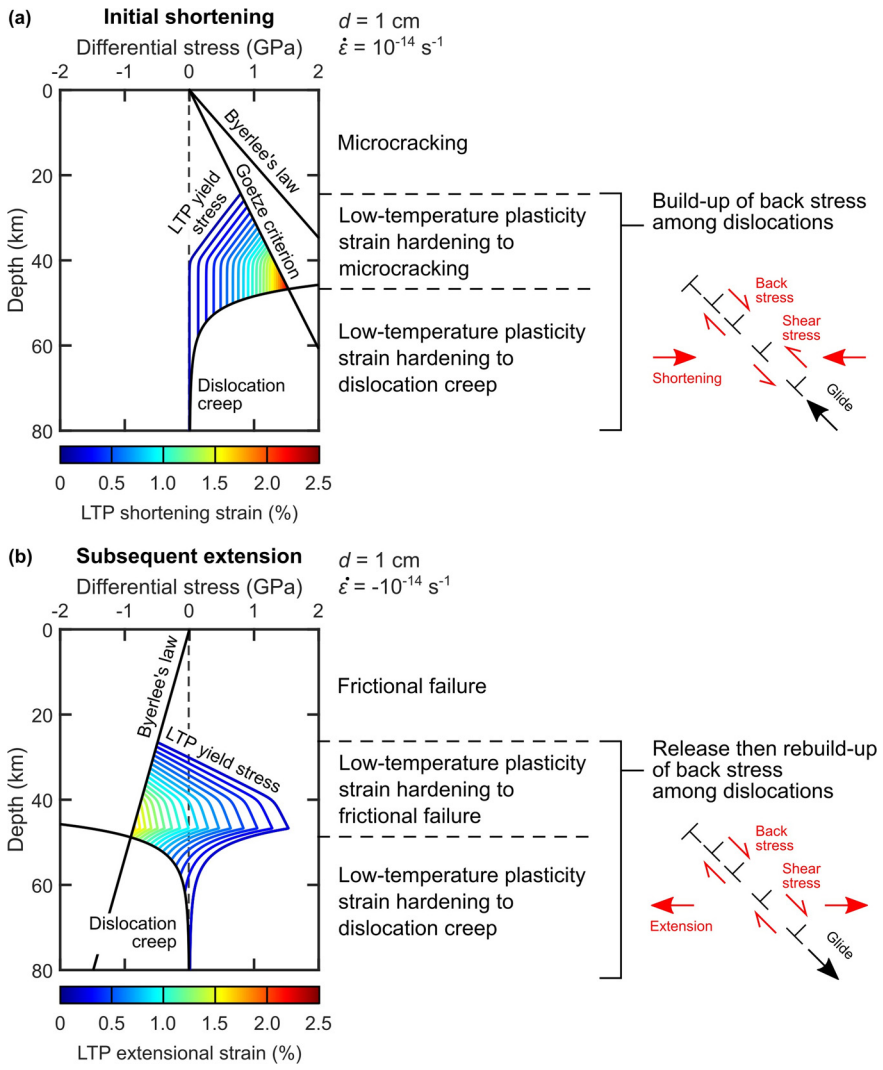

Fig. 9. Evolution of the strength of oceanic lithosphere due to kinematic hardening resulting from back stresses among dislocations. Strength profiles are calculated for (a) an initial phase of shortening and (b) a subsequent phase of extension, both at absolute strain rates ($\dot{\varepsilon}$) of 10^{-14} s^{-1} in dry olivine with a grain size (d) of 1 cm. Stresses were calculated using constitutive equations for low-temperature plasticity (LTP) (Hansen et al., 2019), dislocation creep (Hirth and Kohlstedt, 2003), opening of microcracks following the Goetze criterion (Kohlstedt et al., 1995), and sliding on fractures following Byerlee's law (Byerlee, 1978; Burov, 2011). Compressional stresses are positive and tensional stresses are negative. The temperature profile was calculated for a mantle potential temperature of 1300 °C and 80-Myr-old crust (Turcotte and Schubert, 2014, pp. 185–187). Depth ranges are divided into regimes characterised by particular sequences of deformation mechanisms and schematics indicate the dislocation configurations associated with (a) generation and (b) release of back stress.

5. Conclusions

The microstructures of samples deformed at room temperature in D-DIA and nanoindentation experiments record the microphysical processes of strain hardening during low-temperature plasticity of olivine. Partial dislocations and changes in dislocation density across the intersections of slip bands suggest that short-range interactions impede dislocation glide. However, the presence of intragranular stress heterogeneities with magnitudes on the order of one gigapascal, revealed by HR-EBSD, are consistent with aspects of the mechanical data, including the Bauschinger effect, in indicating that long-range interactions among dislocations are the dominant cause of strain hardening. The results support the parameterisation of strain hardening in terms of accumulation of back stress among dislocations and potentially explain differences in the strength of a lithospheric plate in different tectonic settings. New calculations of the evolution of lithospheric strength suggest that back stresses impart significant mechanical anisotropy to deformed lithosphere that is an important consideration for geodynamic models involving complex strain paths. The stress heterogeneities associated with slip bands also provide new criteria to identify the occurrence of low-temperature plasticity and associated strain hardening in natural samples and thereby test predictions of its occurrence from laboratory-based and geophysical models.

Declaration of competing interest

The authors declare that they have no known competing financial interests or personal relationships that could have appeared to influence the work reported in this paper.

Acknowledgements

We are grateful for the efficient and excellent technical assistance of Haiyan Chen at beamline 6-BM-B at the Advanced Photon Source. We are also thankful for fabrication of assembly parts by Kurt Leinenweber, Jamie Long, and James King. This research was supported by Natural Environment Research Council grants NE/M000966/1 to LNH, AJW, and DW and 1710DG008/JC4 to LNH

and AJW; European Plate Observing System Transnational Access grant EPOS-TNA-MSL 2018-022 to LNH; Advanced Photon Source General User Proposal 55176 to LNH, DLG, and WBD; and National Science Foundation Awards EAR-1361319 to WBD, EAR-1625032 to JMW, and EAR-1806791 to KMK. Data in this paper can be accessed from GFZ Data Services (dataservices.gfz-potsdam.de/portal/).

References

Abramson, E.H., Brown, J.M., Slutsky, L.J., Zaug, J., 1997. The elastic constants of San Carlos olivine to 17 GPa. J. Geophys. Res., Solid Earth 102, 12253–12263. https://doi.org/10.1029/97jb00682.

Audet, P., Bürgmann, R., 2011. Dominant role of tectonic inheritance in supercontinent cycles. Nat. Geosci. 4, 184–187. https://doi.org/10.1038/ngeo1080.

Audet, P., Mareschal, J.-C., 2004. Anisotropy of the flexural response of the lithosphere in the Canadian Shield. Geophys. Res. Lett. 31, L20601. https://doi.org/10.1029/2004GL021080.

Britton, T.B., Jiang, J., Guo, Y., Vilalta-Clemente, A., Wallis, D., Hansen, L.N., Winkelmann, A., Wilkinson, A.J., 2016. Tutorial: Crystal orientations and EBSD — Or which way is up? Mater. Charact. 117, 113–126. https://doi.org/10.1016/j.matchar.2016.04.008.

Britton, T.B., Wilkinson, A.J., 2012. High resolution electron backscatter diffraction measurements of elastic strain variations in the presence of larger lattice rotations. Ultramicroscopy 114, 83–95. https://doi.org/10.1016/j.ultramic.2012.01.004.

Britton, T.B., Wilkinson, A.J., 2011. Measurement of residual elastic strain and lattice rotations with high resolution electron backscatter diffraction. Ultramicroscopy 111, 1395–1404. https://doi.org/10.1016/j.ultramic.2011.05.007.

Buck, W.R., Lavier, L.L., Choi, E., 2015. Magma explains low estimates of lithospheric strength based on flexure of ocean island loads. In: EGU General Assembly, p. 14525.

Buffett, B.A., Becker, T.W., 2012. Bending stress and dissipation in subducted lithosphere. J. Geophys. Res., Solid Earth 117, B05413. https://doi.org/10.1029/2012jb009205.

Burov, E.B., 2011. Rheology and strength of the lithosphere. Mar. Pet. Geol. 28, 1402–1443. https://doi.org/10.1016/j.marpetgeo.2011.05.008.

Byerlee, J., 1978. Friction of rocks. Pure Appl. Geophys. 116, 615–626.

Carter, N.L., Ave'lallemant, H.G., 1970. High temperature flow of dunite and peridotite. Geol. Soc. Am. Bull. 81, 2181–2202. https://doi.org/10.1130/0016-7606(1970)81[2181:htfoda]2.0.co;2.

De Bresser, J.H.P., 2002. On the mechanism of dislocation creep of calcite at high temperature: inferences from experimentally measured pressure sensitivity and strain rate sensitivity of flow stress. J. Geophys. Res., Solid Earth 107, ECV4-1–ECV4-16. https://doi.org/10.1029/2002JB001812.

Druiventak, A., Matysiak, A., Renner, J., Trepmann, C.A., 2012. Kick-and-cook experiments on peridotite: simulating coseismic deformation and post-seismic creep. Terra Nova 24, 62–69. https://doi.org/10.1111/j.1365-3121.2011.01038.x.

Druiventak, A., Trepmann, C.A., Renner, J., Hanke, K., 2011. Low-temperature plasticity of olivine during high stress deformation of peridotite at lithospheric conditions — an experimental study. Earth Planet. Sci. Lett. 311, 199–211. https://doi.org/10.1016/j.epsl.2011.09.022.

Drury, M., 1991. Hydration-induced climb dissociation of dislocations in naturally deformed mantle olivine. Phys. Chem. Miner. 18, 106–116. https://doi.org/10.1007/bf00216603.

Durham, W.B., Goetze, C., 1977. Plastic flow of oriented single crystals of olivine: 1. Mechanical data. J. Geophys. Res. 82, 5737–5753. https://doi.org/10.1029/jb082i036p05737.

Durinck, J., Devincre, B., Kubin, L., Cordier, P., 2007. Modeling the plastic deformation of olivine by dislocation dynamics simulations. Am. Mineral. 92, 1346–1357. https://doi.org/10.2138/am.2007.2512.

England, P., Houseman, G., 1986. Finite strain calculations of continental deformation: 2. Comparison with the India-Asia Collision Zone. J. Geophys. Res., Solid Earth 91, 3664–3676. https://doi.org/10.1029/jb091ib03p03664.

England, P., Molnar, P., 2015. Rheology of the lithosphere beneath the central and western Tien Shan. J. Geophys. Res., Solid Earth 120, 3803–3823. https://doi.org/10.1002/2014jb011733.

Essmann, U., Mughrabi, H., 1979. Annihilation of dislocations during glide at low temperatures. In: Strength of Metals and Alloys 2, pp. 1101–1106.

Gaboriaud, R.J., Darot, M., Gueguen, Y., Woirgard, J., 1981. Dislocations in olivine indented at low temperatures. Phys. Chem. Miner. 7, 100–104. https://doi.org/10.1007/bf00309460.

Guo, Y., Britton, T.B., Wilkinson, A.J., 2014. Slip band–grain boundary interactions in commercial-purity titanium. Acta Mater. 76, 1–12. https://doi.org/10.1016/j.actamat.2014.05.015.

Hansen, L.N., Kumamoto, K.M., Thom, C.A., Wallis, D., Durham, W.B., Goldsby, D.L., Breithaupt, T., Meyers, C.D., Kohlstedt, D.L., 2019. Low-temperature plasticity in olivine: grain size, strain hardening, and the strength of the lithosphere. J. Geophys. Res., Solid Earth 124, 5427–5449. https://doi.org/10.1029/2018jb016736.

Hansen, L.N., Zimmerman, M.E., Kohlstedt, D.L., 2011. Grain boundary sliding in San Carlos olivine: flow law parameters and crystallographic-preferred orientation. J. Geophys. Res. 116, B08201. https://doi.org/10.1029/2011jb008220.

Hirth, G., Kohlstedt, D.L., 2003. Rheology of the upper mantle and the mantle wedge: a view from the experimentalists. In: Eiler, J. (Ed.), Geophysical Monograph Series, vol. 38. American Geophysical Union, Washington, DC, pp. 83–105.

Hunter, J., Watts, A.B., 2016. Gravity anomalies, flexure and mantle rheology seaward of circum-Pacific trenches. Geophys. J. Int. 207, 288–316. https://doi.org/10.1093/gji/ggw275.

Idrissi, H., Bollinger, C., Boioli, F., Schryvers, D., Cordier, P., 2016. Low-temperature plasticity of olivine revisited with in situ TEM nanomechanical testing. Sci. Adv. 2, e1501671. https://doi.org/10.1126/sciadv.1501671.

Kalidindi, S.R., Pathak, S., 2008. Determination of the effective zero-point and the extraction of spherical nanoindentation stress–strain curves. Acta Mater. 56, 3523–3532. https://doi.org/10.1016/j.actamat.2008.03.036.

Kartal, M.E., Kiwanuka, R., Dunne, F.P.E., 2015. Determination of sub-surface stresses at inclusions in single crystal superalloy using HR-EBSD, crystal plasticity and inverse eigenstrain analysis. Int. J. Solids Struct. 67–68, 27–39. https://doi.org/10.1016/j.ijsolstr.2015.02.023.

Kassner, M.E., Geantil, P., Levine, L.E., 2013. Long range internal stresses in single-phase crystalline materials. Int. J. Plast. 45, 44–60. https://doi.org/10.1016/j.ijplas.2012.10.003.

Kirby, J.F., Swain, C.J., 2014. On the robustness of spectral methods that measure anisotropy in the effective elastic thickness. Geophys. J. Int. 199, 391–401. https://doi.org/10.1093/gji/ggu265.

Kocks, U.F., Mecking, H., 2003. Physics and phenomenology of strain hardening: the FCC case. Prog. Mater. Sci. 48, 171–273. https://doi.org/10.1016/s0079-6425(02)00003-8.

Kohlstedt, D.L., Evans, B., Mackwell, S.J., 1995. Strength of the lithosphere: constraints imposed by laboratory experiments. J. Geophys. Res., Solid Earth 100, 17587–17602. https://doi.org/10.1029/95jb01460.

Kuhlmann-Wilsdorf, D., Laird, C., 1979. Dislocation behavior in fatigue II. Friction stress and back stress as inferred from an analysis of hysteresis loops. Mater. Sci. Eng. 37, 111–120. https://doi.org/10.1016/0025-5416(79)90074-0.

Kumamoto, K.M., Thom, C.A., Wallis, D., Hansen, L.N., Armstrong, D.E.J., Warren, J.M., Goldsby, D.L., Wilkinson, A.J., 2017. Size effects resolve discrepancies in 40 years of work on low-temperature plasticity in olivine. Sci. Adv. 3, e1701338. https://doi.org/10.1126/sciadv.1701338.

Matysiak, A.K., Trepmann, C.A., 2012. Crystal-plastic deformation and recrystallization of peridotite controlled by the seismic cycle. Tectonophysics 530–531, 111–127. https://doi.org/10.1016/j.tecto.2011.11.029.

Mei, S., Suzuki, A.M., Kohlstedt, D.L., Dixon, N.A., Durham, W.B., 2010. Experimental constraints on the strength of the lithospheric mantle. J. Geophys. Res. 115, B08204. https://doi.org/10.1029/2009jb006873.

Meyer, G.G., Brantut, N., Mitchell, T.M., Meredith, P.G., 2019. Fault reactivation and strain partitioning across the brittle-ductile transition. Geology 47, 1127–1130. https://doi.org/10.1130/G46516.1.

Montagnat, M., Weiss, J., Chevy, J., Duval, P., Brunjail, H., Bastie, P., Gil Sevillano, J., 2006. The heterogeneous nature of slip in ice single crystals deformed under torsion. Philos. Mag. 86, 4259–4270. https://doi.org/10.1080/14786430500452602.

Mussi, A., Cordier, P., Demouchy, S., Hue, B., 2017. Hardening mechanisms in olivine single crystal deformed at 1090 °C: an electron tomography study. Philos. Mag. 97, 3172–3185. https://doi.org/10.1080/14786435.2017.1367858.

Nes, E., 1997. Modelling of work hardening and stress saturation in FCC metals. Prog. Mater. Sci. 41, 129–193. https://doi.org/10.1016/s0079-6425(97)00032-7.

Nix, W.D., Gao, H., 1998. Indentation size effects in crystalline materials: a law for strain gradient plasticity. J. Mech. Phys. Solids 46, 411–425. https://doi.org/10.1016/s0022-5096(97)00086-0.

Phakey, P., Dollinger, G., Christie, J., 1972. Transmission electron microscopy of experimentally deformed olivine crystals. In: Heard, H.C., Borg, I.Y., Carter, N.L., Raleigh, C.B. (Eds.), Flow and Fracture of Rocks 16. In: Geophysical Monograph Series. American Geophysical Union, pp. 117–138.

Poirier, J.P., 1981. Martensitic olivine-spinel transformation and plasticity of the mantle transition zone. In: Anelasticity in the Earth 4.

Poirier, J.P., Vergobbi, B., 1978. Splitting of dislocations in olivine, cross-slip-controlled creep and mantle rheology. Phys. Earth Planet. Inter. 16, 370–378. https://doi.org/10.1016/0031-9201(78)90075-4.

Simons, F.J., van der Hilst, R.D., 2003. Seismic and mechanical anisotropy and the past and present deformation of the Australian lithosphere. Earth Planet. Sci. Lett. 211, 271–286. https://doi.org/10.1016/s0012-821x(03)00198-5.

Swain, M.V., Hagan, J.T., 1976. Indentation plasticity and the ensuing fracture of glass. J. Phys. D, Appl. Phys. 9, 2201–2214. https://doi.org/10.1088/0022-3727/9/15/011.

Turcotte, D.L., Schubert, G., 2014. Geodynamics. Cambridge University Press, pp. 185–187.

Underwood, E.E., 1970. Quantitative Stereology. Addison-Wesley, pp. 80–93.

van Heck, H.J., Tackley, P.J., 2008. Planforms of self-consistently generated plates in 3D spherical geometry. Geophys. Res. Lett. 35, L19312. https://doi.org/10.1029/2008gl035190.

Walcott, R.I., 1970. Flexural rigidity, thickness, and viscosity of the lithosphere. J. Geophys. Res. 75, 3941–3954. https://doi.org/10.1029/jb075i020p03941.

Wallis, D., Hansen, L.N., Ben Britton, T., Wilkinson, A.J., 2017. Dislocation interactions in olivine revealed by HR-EBSD. J. Geophys. Res., Solid Earth 122, 7659–7678. https://doi.org/10.1002/2017jb014513.

Wallis, D., Hansen, L.N., Ben Britton, T., Wilkinson, A.J., 2016. Geometrically necessary dislocation densities in olivine obtained using high-angular resolution electron backscatter diffraction. Ultramicroscopy 168, 34–45. https://doi.org/10.1016/j.ultramic.2016.06.002.

Wallis, D., Hansen, L.N., Britton, T.B., Wilkinson, A.J., 2019. High-angular resolution electron backscatter diffraction as a new tool for mapping lattice distortion in geological minerals. J. Geophys. Res., Solid Earth 124, 6337–6358. https://doi.org/10.1029/2019jb017867.

Watts, A.B., Zhong, S.J., Hunter, J., 2013. The behavior of the lithosphere on seismic to geologic timescales. Annu. Rev. Earth Planet. Sci. 41, 443–468. https://doi.org/10.1146/annurev-earth-042711-105457.

Wessel, P., 1992. Thermal stresses and the bimodal distribution of elastic thickness estimates of the oceanic lithosphere. J. Geophys. Res. 97, 14177–14193. https://doi.org/10.1029/92jb01224.

Wilkinson, A.J., Meaden, G., Dingley, D.J., 2006. High-resolution elastic strain measurement from electron backscatter diffraction patterns: new levels of sensitivity. Ultramicroscopy 106, 307–313. https://doi.org/10.1016/j.ultramic.2005.10.001.

Zhong, S., Watts, A.B., 2013. Lithospheric deformation induced by loading of the Hawaiian Islands and its implications for mantle rheology. J. Geophys. Res., Solid Earth 118, 6025–6048. https://doi.org/10.1002/2013jb010408.